Industrial Chemistry & Materials

ROYAL SOCIETY OF CHEMISTRY

PAPER

View Article Online
View Journal

Cite this: DOI: 10.1039/d5im00266d

Efficient separation of 1,5-dimethyl-2-pyrrolidone from *N*-methylpyrrolidone enabled by pore confinement

Rongkai Cui,†[a] Minlei Yin,†[ad] Xiaoyan Chen,[c] Xiaoyu Lou,[a] Chen Yang,[a] Ting Qiu *[ab] and Jie Chen *[a]

To achieve sub-angstrom separation of *N*-methylpyrrolidone and 1,5-dimethyl-2-pyrrolidone, cyclodextrin-derived carbon materials with distinct pore environments and surface functionalities were synthesized *via* hydrothermal carbonization and high-temperature pyrolysis. Three types of carbons were obtained: non-porous carbons rich in surface functionalities, carbons with both functionalities and microporous structures, and carbons with limited functionalities but diverse micropore environments. Systematic adsorption experiments, supported by density functional theory and molecular dynamics simulations, were conducted to establish the structure–performance relationships. The results demonstrate that surface functionalities alone are insufficient for separation, whereas pore confinement is the decisive factor. A 7.3 Å pore was identified as the optimal confinement space, providing the strongest thermodynamic interactions and the fastest diffusion kinetics, thereby enabling highly selective adsorption of 1,5-dimethyl-2-pyrrolidone from *N*-methylpyrrolidone. This work not only clarifies the pore formation mechanism of cyclodextrin-derived carbons but also highlights precise pore-size tuning as a paradigm for sub-angstrom molecular separation, offering theoretical guidance for the design of advanced adsorbent materials.

Keywords: Wet electronic chemicals; Purification; Adsorption mechanism; Carbon material; *N*-Methylpyrrolidone; 1,5-Dimethyl-2-pyrrolidone.

Received 25th September 2025,
Accepted 12th November 2025

DOI: 10.1039/d5im00266d

rsc.li/icm

1 Introduction

The competitiveness of the semiconductor industry hinges critically on the purification of wet electronic chemicals, with ultra-high-purity production technologies representing a central focus.[1–3] Among these chemicals, *N*-methylpyrrolidone (NMP) plays a pivotal role in chip fabrication, as its purity directly determines the fidelity of photolithography, etching, and surface cleaning processes.[4] To ensure safety and compatibility in advanced device manufacturing, the organic purity of NMP must surpass 99.9%.[5,6] The industrial synthesis of NMP is conventionally carried out *via* the reaction of γ-butyrolactone with methylamine. Under conditions of approximately 250 °C and 5.88 MPa, the primary intermediate, 4-hydroxy-1-methylbutanamide, is selectively formed. However, incomplete dehydration or nucleophilic attack of methylamine at non-α-carbonyl sites results in the formation of positional isomers of 1,5-dimethyl-2-pyrrolidone (DMP) during cyclization.[7] Excess methylamine promotes over-methylation of the nitrogen in the intermediate, resulting in the formation of DMP impurities. In semiconductor wafer-cleaning processes, water rinsing is conventionally employed to remove organic residues while maintaining wafer surface integrity. Nevertheless, the low solubility of DMP impedes its effective removal, resulting in persistent residues on wafer surfaces. These residues compromise lithographic accuracy, accelerate equipment fouling, and ultimately jeopardize operational stability and production efficiency.[8,9] Thus, developing efficient methods for the selective removal of DMP from NMP is of critical importance, not only for enhancing device yield and reducing manufacturing costs but also for extending equipment lifespan and enabling high-throughput semiconductor fabrication.

[a] *State Key Laboratory of Green and Efficient Development of Phosphorus Resources, Engineering Research Center of Reactive Distillation, Fujian Province University, College of Chemical Engineering, Fuzhou University, Fuzhou 350108, China. E-mail: tingqiu@fzu.edu.cn, jiechen@fzu.edu.cn*
[b] *Qingyuan Innovation Laboratory, Quanzhou 362801, P. R. China*
[c] *Fuzhou University International Joint Laboratory of Thermochemical Conversion of Biomass, Fuzhou University, Fuzhou, 350108, China*
[d] *School of Chemical Engineering and Dyeing Engineering, Henan University of Engineering, Zhengzhou 450007, China*
† These authors contributed equally to this work.

The separation of DMP from NMP is predominantly achieved *via* vacuum distillation. However, with boiling points of 203 °C (NMP) and 215 °C (DMP), both compounds exhibit high thermal stability, and their relative volatility under reduced pressure approaches unity. This near-azeotropic behavior renders conventional distillation inherently inefficient, highlighting the urgent need for innovative separation technologies to meet the stringent purity requirements of next-generation semiconductor manufacturing.[10,11]

Adsorption has emerged as a promising strategy for separating structurally similar species by exploiting subtle differences in molecular physicochemical properties through rational adsorbent design.[12–14] To the best of our knowledge, no prior studies have reported the separation of DMP from NMP. Density functional theory (DFT) calculations were conducted using Gaussian16 to optimize the geometries of NMP and its major impurity, DMP. The calculated molecular dimensions were 3.4 × 5.0 × 6.2 Å^3 for NMP and 3.9 × 5.9 × 6.5 Å^3 for DMP. Notably, the dimensional differences between NMP and impurities such as γ-butyrolactone (GBL) and DMP are less than 1 Å—far below the threshold for conventional pore-size sieving—rendering traditional adsorbents ineffective for selective removal. Therefore, the selective and efficient separation of DMP from NMP remains a significant challenge.

In molecular adsorption mechanisms, the pore confinement effect enhances interactions between pore walls and molecules, thereby improving adsorption selectivity for molecules with sub-ångström-scale size differences.[15–17] This design strategy effectively addresses the poor selectivity of adsorbents toward DMP in NMP. Thus, by leveraging the pore confinement effect, precise pore size control provides a promising pathway for overcoming the challenge of separating DMP from NMP.[18,19] Porous carbons serve as a prototypical platform for studying the interaction between pore confinement and molecular adsorption.[20,21] By virtue of their tunable pore sizes, carbons can be engineered to match the molecular dimensions of DMP, thereby enhancing selective adsorption through confinement. Given the molecular size disparity between NMP and DMP, size exclusion predominantly occurs within the micropore range (0–20 Å), where the slightly larger DMP experiences pronounced confinement, enabling preferential adsorption over NMP.[22] The selective adsorption of DMP from NMP remains insufficiently explored, and the design principles for confined micropore environments suitable for such separations remain poorly understood. Thus, rational control over micropore architectures in carbons offers a promising approach for developing advanced adsorbents for efficient DMP removal.

In this study, cyclodextrin (CD) was used as a carbon precursor to synthesize a series of structurally diverse carbons through controlled preparation methods. Hydrothermal carbonization generated materials with abundant surface functional groups but without well-defined porosity, enabling systematic evaluation of functionality-dependent DMP adsorption. High-temperature pyrolysis of the hydrothermal carbons produced hybrid materials integrating abundant surface groups with well-developed micropore networks, offering insights into the synergistic effects of functionalities and confinement. In contrast, direct pyrolysis produced carbons with sparse surface functionalities but distinct micropore environments, highlighting the role of confinement in DMP uptake. To elucidate the molecular-level adsorption mechanisms, DFT calculations were conducted to quantify the adsorption energy differences of hydroxyl and carboxyl groups toward NMP and DMP. Coupled with Multiwfn and VMD analyses, these results provided insights into the interaction modes between functional groups and adsorbates. Complementary molecular dynamics (MD) simulations further demonstrated the diffusion characteristics across different pore sizes, providing insights into the selective adsorption of DMP in NMP from both thermodynamic and kinetic perspectives. Collectively, these findings provide key design principles for carbon-based adsorbents capable of efficiently removing DMP from NMP.

2 Results and discussion

2.1 Designs and DFT calculation confirmation

DFT calculations reveal molecular dimensions of 3.4 × 5.0 × 6.2 Å^3 for NMP and 3.9 × 5.9 × 6.5 Å^3 for DMP, with DMP exhibiting larger dimensions than NMP. To achieve effective DMP adsorption from NMP, the adsorbent pore size must exceed 5.9 Å to accommodate DMP molecules. However, since DMP is larger than NMP, size-based sieving alone is insufficient for selective DMP adsorption. Consequently, molecular structural differences must be considered in adsorbent design. Structural analysis shows that DMP contains an additional methyl group compared to NMP, conferring it with hydrogen-bond donor capability. This property provides a molecular foundation for designing hydrogen-bond acceptor materials that enhance DMP adsorption and enable selective separation. Nevertheless, systematic studies and theoretical frameworks defining the optimal pore size range for DMP remain insufficient, especially when selectivity requirements conflict with size-based separation mechanisms. The π-electron-rich nature of porous carbon materials allows them to act as hydrogen-bond acceptors, enhancing molecular recognition with DMP *via* C–H···π interactions. Furthermore, the continuous tunability of pore sizes in these materials offers a novel strategy for efficient DMP separation. Through precise pore dimension engineering of carbon materials, their compatibility with DMP can be optimized, enabling selective DMP adsorption from NMP (Scheme 1).

2.2 Structural characterization of adsorbed materials

2.2.1 Structural analysis of hydrothermal carbon materials. To investigate the role of surface functional groups in DMP

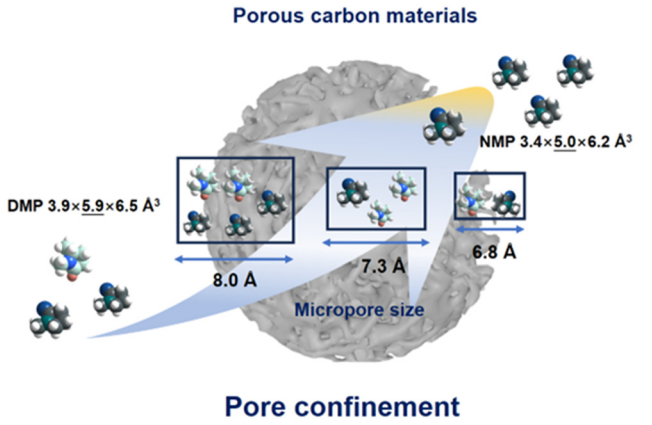

Scheme 1 Schematic illustration of the mechanism for separating DMP from NMP *via* the pore confinement effect.

adsorption from NMP, hydrothermal carbons (α-CD-230, β-CD-230, and γ-CD-230) were synthesized from α-cyclodextrin (α-CD), β-cyclodextrin (β-CD), and γ-cyclodextrin (γ-CD), respectively. Nitrogen adsorption–desorption isotherms were used to characterize the pore structures of these materials. As shown in Fig. 1a and S2, all hydrothermal carbons exhibited negligible nitrogen uptake, and pore size analysis revealed no microporosity. The pore volumes of α-CD-230, β-CD-230, and γ-CD-230 were measured as 0.09 $cm^3\ g^{-1}$, 0.09 $cm^3\ g^{-1}$, and 0 $cm^3\ g^{-1}$, respectively, with surface areas of 7 $m^2\ g^{-1}$, 0 $m^2\ g^{-1}$, and 2 $m^2\ g^{-1}$ (Table S1). These findings demonstrate that cyclodextrin-derived hydrothermal carbons exhibit minimal surface area and porosity, likely due to dehydration and condensation of cyclodextrin during hydrothermal carbonization.[23] This process leads to the formation of amorphous carbon without pore-creating mechanisms, resulting in dense rather than porous structures. FT-IR spectroscopy was subsequently employed to analyze the surface functional groups of α-CD-230, β-CD-230, and γ-CD-230. FT-IR spectra exhibited distinct absorption bands at 3415 cm^{-1}, 1596 cm^{-1}, and 1368 cm^{-1} (Fig. 1b). The broad band at 3415 cm^{-1} is attributed to O–H stretching vibrations,[24,25] while the peaks at 1596 cm^{-1} and 1368 cm^{-1} correspond to C=O stretching vibrations of carboxyl (–COOH) groups. These characteristic peaks were consistently detected in all three materials, confirming the presence of hydroxyl (–OH) and carboxyl (–COOH) functional groups on the carbon surfaces.

2.2.2 Structural analysis of activated hydrothermal carbon materials. To investigate the effect of pore confinement on DMP adsorption in NMP, hydrothermal carbons with distinct pore structures (α-CD-230, β-CD-230, and γ-CD-230) were activated at 800 °C. The resulting materials were characterized by nitrogen adsorption–desorption analysis (Fig. 1c and S3), with their specific surface areas and total pore volumes summarized in Table S3. After activation, the specific surface areas of α-CD-800, β-CD-800, and γ-CD-800 were 389 $m^2\ g^{-1}$, 392 $m^2\ g^{-1}$, and 362 $m^2\ g^{-1}$, respectively, with total pore volumes of 0.25 $cm^3\ g^{-1}$, 0.26 $cm^3\ g^{-1}$, and 0.25 $cm^3\ g^{-1}$. All three materials exhibited hierarchical pore structures comprising micropores, mesopores, and macropores. Micropore analysis revealed that α-CD-800 predominantly contained 6.8 Å micropores with a minor fraction of 10.9 Å micropores, while β-CD-800 was dominated by 7.3 Å micropores along with smaller contributions from 10 Å and 13.6 Å micropores. γ-CD-800 exhibited micropores of 7.3 Å, 8.0 Å, and 10.9 Å, with the 10.9 Å pores being the least abundant. The micropore volumes of all three materials were comparable, ranging from 0.14 to 0.15 $cm^3\ g^{-1}$. Comparison of the pre- and post-activation states confirmed that high-temperature activation effectively transformed the hydrothermal carbons from low-surface-area, nonporous precursors into materials with substantial surface areas and well-developed hierarchical pore structures. This demonstrates that activation at elevated temperatures induces significant microstructural evolution, thereby enhancing surface area and generating a complex pore network essential for improving adsorption performance. FT-IR spectroscopy was performed on α-CD-800 and γ-CD-800 to analyze their surface functional groups. As shown in Fig. S4, distinct absorption peaks appeared at 3434 cm^{-1}, 1610 cm^{-1}, and 1364 cm^{-1}. The band at 3434 cm^{-1} corresponds to –OH stretching vibrations, while those at 1610 cm^{-1} and 1364 cm^{-1} are assigned to –COOH group stretching vibrations. These features were consistently observed in both materials, confirming the presence of –OH and –COOH functional groups on the adsorbent surfaces.

Elemental analysis of α-CD-800, β-CD-800, and γ-CD-800 (Table S4) revealed significant compositional changes after activation. The carbon content increased to over 90 wt%, while hydrogen and oxygen contents decreased markedly. Notably, the oxygen content dropped from ~24 wt% to ~6 wt%, primarily due to bound water removal during calcination, which concurrently promoted pore formation. Furthermore, decomposition of amorphous phases in the precursors at elevated temperatures likely contributed to pore development.[26] The microporous structures of α-CD-800, β-CD-800, and γ-CD-800 were characterized by dominant pore sizes ranging from 6.8 to 8.0 Å. Notably, β-CD-800 exhibited a distinctive pore architecture with a secondary micropore peak at 13.6 Å in addition to its primary distribution, resulting in a broader spectrum of primary and secondary micropores compared to α-CD-800 and γ-CD-800. Such structural diversity enables the formation of a wider range of micropore sizes during pyrolysis at different temperatures, which is critical for understanding confinement-driven DMP adsorption in NMP and identifying optimal adsorption pore types.

Based on these findings, β-CD-230 was selected for further investigation, and a series of activation temperatures (500 °C, 600 °C, 700 °C, 800 °C, and 900 °C) were applied to examine micropore evolution. As shown in Fig. S4, carbon materials calcined at 500 °C exhibited negligible surface area, whereas those treated at 600–900 °C showed progressively increasing surface areas, with

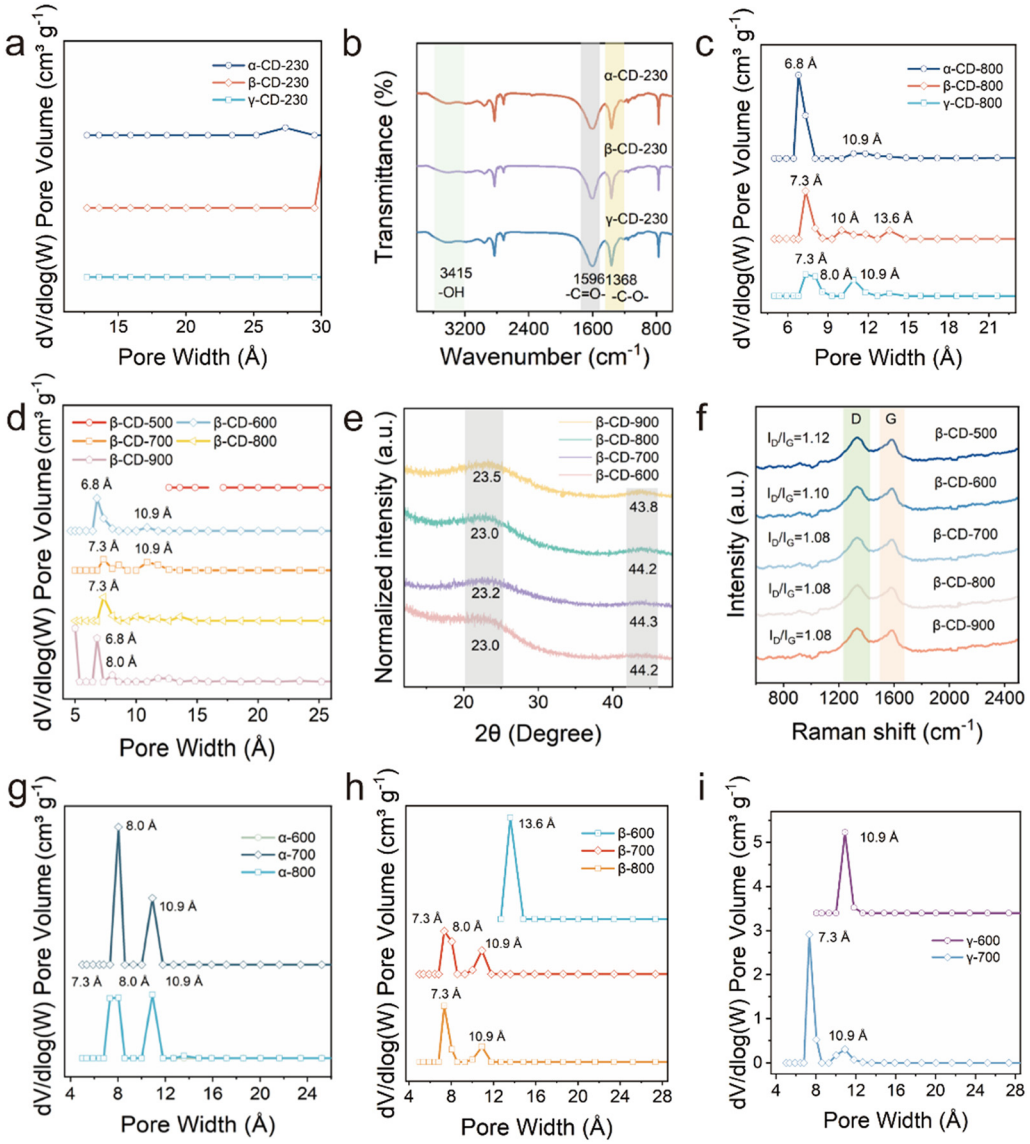

Fig. 1 (a) Pore size distribution curves of α-CD-230, β-CD-230, and γ-CD-230; (b) FT-IR spectra of α-CD-230, β-CD-230 and γ-CD-230; (c) α-CD-800, β-CD-800 and γ-CD-800; (d) β-CD-500, β-CD-600, β-CD-700, β-CD-800 and γ-CD-900 calculated by NLDFT method; (e) PXRD patterns of β-CD-600, β-CD-700, β-CD-800 and β-CD-900; (f) Raman spectra of β-CD-500, β-CD-600, β-CD-700, β-CD-800 and β-CD-900; pore size distribution curves of (g) α-600, α-700, and α-800; (h) β-600, β-700, and β-800. (i) γ-600, and γ-700 calculated by NLDFT method.

micropore volumes rising from 0.13 to 0.21 $cm^3\ g^{-1}$. Pore structure analysis (Table S5) confirmed that β-CD-600, β-CD-700, β-CD-800, and β-CD-900 all possessed hierarchical pore structures. However, at 900 °C, macropores were completely eliminated, leaving only micropores and mesopores. The micropore size distributions of β-CD-500, β-CD-600, β-CD-700, β-CD-800, and β-CD-900 are presented in Fig. 1d and S5. β-CD-500 exhibited no detectable micropores, while β-CD-600 contained predominantly 6.8 Å micropores with a minor fraction at 10.9 Å. β-CD-700 showed nearly equal proportions of 7.3 Å and 10.9 Å micropores. At higher temperatures, β-CD-800 consisted mainly of 7.3 Å micropores, whereas β-CD-900 predominantly exhibited pores smaller than 5 Å. Since both NMP and DMP molecules exceed 5 Å in size, these sub-5 Å pores are ineffective for adsorption and were excluded from further consideration. Within the effective pore size range, β-CD-900 predominantly contained 6.8 Å micropores, along with a minor fraction of 8.0 Å micropores.

The predominant micropore diameters of β-CD-600, β-CD-700, β-CD-800, and β-CD-900 were 6.8 Å, 7.3 Å, 7.3 Å, and 6.8 Å, respectively. As the activation temperature increased, the main micropore diameter of β-CD-230 initially increased and then decreased. Elemental analysis of β-CD-230-derived carbons across activation temperatures from 500–900 °C was conducted to investigate compositional evolution within three thermal regimes: low temperature (≤500 °C), medium-high temperature (500–800 °C), and high temperature (>800 °C). The results (Table S6) revealed that the carbon content increased from 85.84 wt% at 500 °C to 93.29 wt% at 900 °C,

while hydrogen content decreased from 3.31 wt% to 1.03 wt% and oxygen content decreased from 10.59 wt% to 5.03 wt%. During the low-temperature stage, deoxygenation and dehydrogenation were predominant, accompanied by water desorption and surface functional group decomposition, releasing gases such as H_2O, CO, and CO_2. The carbon content of β-CD-230 increased from 71.10 wt% to 85.84 wt%, while hydrogen and oxygen contents decreased from 4.63 wt% to 3.31 wt% and from 24.19 wt% to 10.59 wt%, respectively. Amorphous carbon began to form, although structural defects persisted. In the medium-high temperature regime, the carbon skeleton underwent restructuring, with residual alkyl chains further dehydrogenated into aromatic structures. Concurrently, oxygen-containing functional groups, such as carbonyl and ether groups, were cleaved, resulting in higher carbon proportion and improved purity, yielding a predominantly sp^2-hybridized framework. In the high-temperature regime, the carbon skeleton experienced further rearrangement, accompanied by increased graphitization.[27] Overall, the compositional evolution reflects a transition from a defect- and functional-group-rich structure to a high-purity carbon material. XRD analysis was employed to investigate structural evolution of β-CD-derived carbons synthesized at 600–900 °C (Fig. 1e). The broad feature at ~44° corresponds to the (100) reflection of turbostratic carbon, while the peak near 23° corresponds to the (002) reflection of amorphous graphite-like domains.[28] All samples exhibited low crystallinity, as evidenced by the broadening of the (100) peak. Notably, the (002) reflection intensified with increasing temperature, indicating progressive local ordering within the amorphous matrix. Raman spectroscopy further elucidated graphitization and defect evolution (Fig. 1f). The D band (~1330 cm^{-1}) originates from disordered/defective carbon sites, while the G band (~1558 cm^{-1}) corresponds to sp^2-hybridized graphitic domains.[29] The I_D/I_G ratio decreased from 1.12 to 1.08 with increasing calcination temperature, stabilizing at 1.08 beyond 700 °C. This trend indicates that moderate heating facilitates reorganization of amorphous carbon into more ordered graphitic structures, while above 700 °C, graphitization reaches a plateau with negligible further structural evolution.

2.2.3 Structural analysis of pyrolysis carbon materials. To investigate the effect of micropore confinement on DMP adsorption in NMP while minimizing surface functional group influence, we synthesized carbon materials with tunable microporous environments *via* one-step pyrolysis of cyclodextrins (α-CD, β-CD, and γ-CD) with distinct cavity sizes. Nitrogen adsorption–desorption isotherms of α-CD-derived carbons pyrolyzed at 600, 700, and 800 °C (denoted as α-600, α-700, and α-800) are presented in Fig. 1g and S6. As observed, α-600 exhibited negligible nitrogen uptake, and its micropore size distribution confirmed the absence of microporous structures. The specific surface areas of α-600, α-700, and α-800 were 3, 313, and 418 $m^2\ g^{-1}$, respectively (Table S7), indicating that pyrolysis at 600 °C failed to produce a porous structure, whereas pyrolysis at 700 and 800 °C yielded hierarchical porous structures containing micro-, meso-, and macropores. The micropore volumes of α-700 and α-800 were 0.12 and 0.16 $cm^3\ g^{-1}$, respectively, with α-800 exhibiting the highest surface area. Micropore size analysis further revealed that α-700 was dominated by 8.0 Å micropores with 10.9 Å as a secondary size, while α-800 predominantly contained 7.3, 8.0, and 10.9 Å micropores. These results confirm that pyrolysis temperature effectively tailors micropore structures. Similarly, nitrogen adsorption–desorption measurements of β-CD-derived carbons (β-600, β-700, β-800) showed that β-600 exhibited negligible uptake with a surface area of only 49 $m^2\ g^{-1}$, whereas β-700 and β-800 possessed significantly higher surface areas of 338 and 379 $m^2\ g^{-1}$, respectively (Table S8). Micropore analysis indicated that β-700 was primarily composed of 13.6 Å micropores, while β-800 was dominated by 7.3 Å pores with secondary contributions from 10.9 Å pores (Fig. 1h and S7). For γ-CD-derived carbons (γ-600 and γ-700), nitrogen adsorption–desorption characterization (Fig. 1i and S8) revealed surface areas of 288 and 366 $m^2\ g^{-1}$, respectively (Table S9). Micropore analysis revealed that γ-600 predominantly contained 10.9 Å pores, while γ-700 was enriched in 7.3 Å micropores with 10.9 Å serving as a secondary size. Based on these findings, five carbon materials with distinct micropore structures were identified as suitable candidates for DMP adsorption: α-800 (7.3, 8.0, and 10.9 Å), α-700 (8.0 and 10.9 Å), γ-600 (10.9 Å), β-700 (13.6 Å), and β-800 (7.3 and 10.9 Å).

FT-IR spectroscopy and elemental analysis (EA) were further employed to evaluate surface functional groups. FT-IR spectra (Fig. S9) revealed characteristic peaks at 3129, 1615, and 1400 cm^{-1}, corresponding to –OH and –COOH stretching vibrations, thereby confirming the presence of hydroxyl and carboxyl groups in all five carbons. EA results (Table S10) showed that direct pyrolysis of cyclodextrins yielded carbons with higher carbon content and lower hydrogen and oxygen contents compared to their hydrothermally carbonized counterparts (Table S6). At 800 °C, hydrogen and oxygen were nearly completely removed: α-800 contained 0.69 wt% hydrogen and 0.78 wt% oxygen, while β-800 contained 0.79 wt% hydrogen and 0.99 wt% oxygen. This pronounced decrease indicates negligible surface functional group content in α-800, α-700, γ-600, β-700, and β-800, thereby suggesting that adsorption capacity is governed primarily by pore confinement rather than surface chemistry. In summary, a series of porous carbons with well-defined micropore structures and minimal surface functional groups were successfully synthesized *via* direct pyrolysis of α-CD, β-CD, and γ-CD. Nitrogen physisorption, FT-IR spectroscopy, and elemental analysis confirmed their structural and compositional characteristics, thereby enabling a systematic investigation of pore confinement effects on the selective adsorption of DMP from NMP.

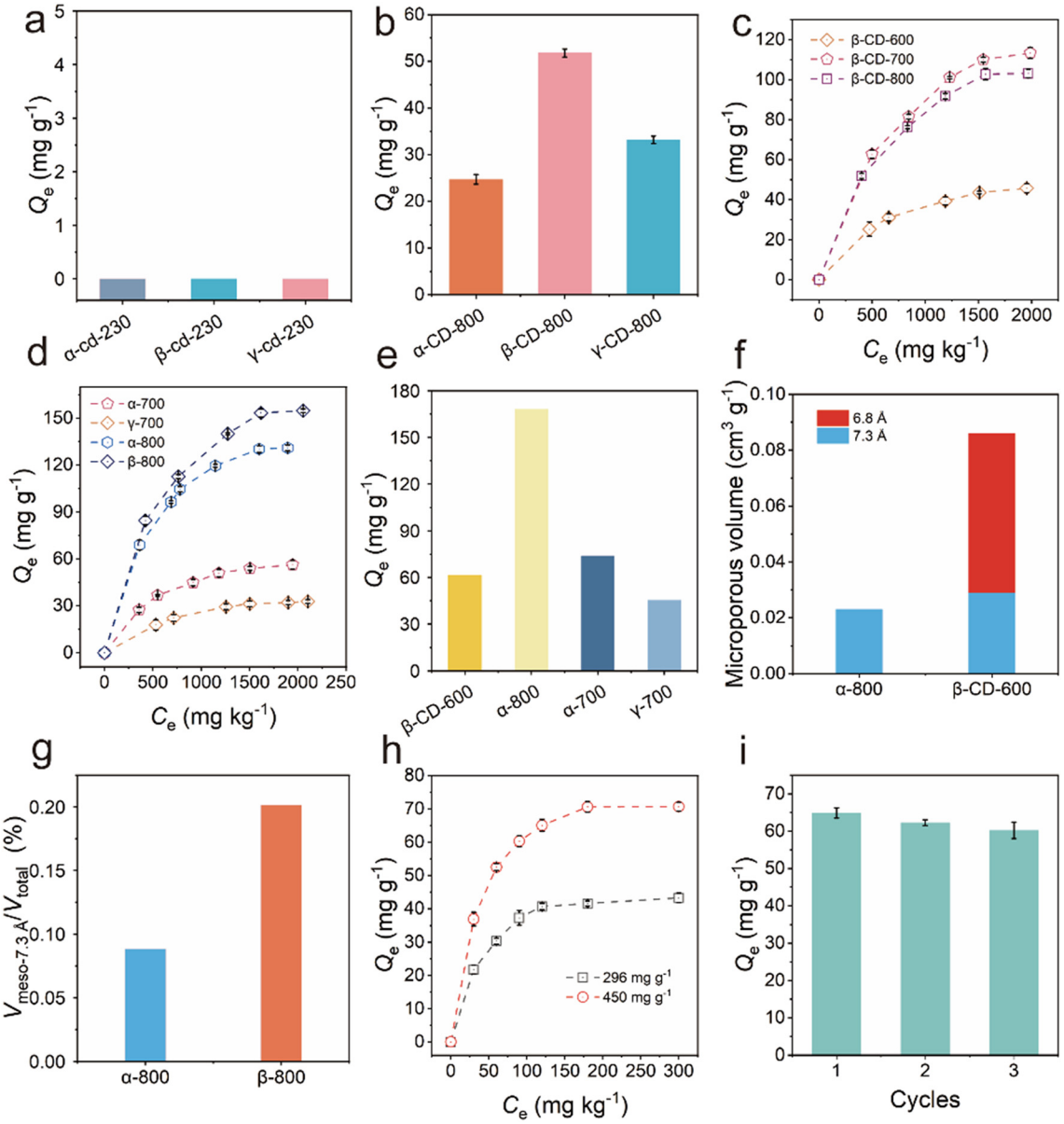

Fig. 2 Adsorption capacities of (a) α-CD-230, β-CD-230 and γ-CD-230 for DMP, (b) α-CD-800, β-CD-800 and γ-CD-800 for DMP; adsorption isotherms of (c) β-CD-600, β-CD-700 and β-CD-800 for DMP in NMP at 25 °C, (d) α-700, γ-700, α-800 and β-800 for DMP in NMP at 25 °C; (e) adsorption capacities of β-CD-600, α-800, α-700 and γ-700 for DMP; (f) pore volume distributions of α-800 and β-CD-600; (g) contribution of 7.3 Å micropores to the total pore volume in α-800 and β-800; (h) adsorption kinetic curves of β-800 for DMP at various concentrations; (i) recyclability studies of β-800.

2.3 Adsorption performance

2.3.1 Impact of surface functional groups on DMP adsorption. To investigate the impact of surface functional groups on DMP adsorption, α-CD-230, β-CD-230, and γ-CD-230—each containing hydroxyl (–OH) and carboxyl (–COOH) groups but lacking pore structures—were selected as adsorbents for this study. The polar functional groups facilitate interaction between the adsorbent and the DMP molecules, promoting DMP diffusion within the material. A series of DMP solutions at varying concentrations were prepared in NMP and tested on the three adsorbents. As shown in Fig. 2a, under varying initial concentrations, the carbon-based adsorbents exhibited negligible DMP uptake in the NMP solution. This indicates that while polar functional groups such as –OH and –COOH were introduced, these groups were insufficient for effective DMP recognition and selective adsorption. The lack of selectivity can be attributed to the high structural similarity between NMP and DMP, which differ only by a single methyl group. This structural similarity restricts selective adsorption due to the analogous chemical environments of both molecules, thereby limiting functional group interactions. Nitrogen adsorption–desorption tests confirmed that all materials were

nonporous, with adsorption occurring primarily on the two-dimensional surface. Consequently, both DMP and NMP resided in nearly identical chemical environments, precluding molecular discrimination. The absence of pore-selective effects further underscores that nonporous carbon materials, even with surface functional groups, cannot distinguish between structurally similar DMP and NMP molecules. Therefore, to achieve selective DMP adsorption, the adsorbent microenvironment must be precisely engineered to create distinct local environments for DMP and NMP, thereby enhancing their differential recognition and binding.

2.3.2 Verification of the role of pore structure in selective adsorption. Previous studies have demonstrated that surface functional groups on carbon materials do not play a dominant role in governing DMP adsorption from NMP. In this section, we investigate the critical role of pore structure in selective adsorption. By designing carbon materials with tailored pore structures featuring specific pore sizes and chemical environments, we aim to leverage the pore confinement effect to enhance molecular recognition and selective adsorption. The adsorption performance of α-CD-800, β-CD-800, and γ-CD-800, which possess abundant functional groups and well-defined microporous structures, was evaluated. Adsorption tests were conducted with an initial DMP concentration of 460 mg kg^{-1}, as shown in Fig. 2b. The selective adsorption capacities for DMP were 24.7, 51.8, and 33.2 mg g^{-1} for α-CD-800, β-CD-800, and γ-CD-800, respectively. In contrast, α-CD-230, β-CD-230, and γ-CD-230 exhibited negligible adsorption, highlighting the markedly superior performance of α-CD-800, β-CD-800, and γ-CD-800, which were synthesized *via* pyrolysis at 800 °C. The pore structures of α-CD-800, β-CD-800, and γ-CD-800 differ significantly from those of α-CD-230, β-CD-230, and γ-CD-230, with this structural variation serving as the key determinant of their distinct DMP adsorption performances. These findings further confirm that tailoring pore structures is essential for achieving selective DMP adsorption. Additionally, the differences in micropore size distribution constitute the primary determinants of the varying adsorption capacities of α-CD-800, β-CD-800, and γ-CD-800.

2.3.3 Pore confinement effect of carbon materials. The pore confinement effect manifests when adsorbent pore sizes approach molecular dimensions, where spatial restrictions regulate adsorption selectivity through geometric sieving and synergistic interactions at the molecule–pore interface, including polarization, molecular orientation, and entropic contributions, collectively enhancing selectivity.[30,31] To identify optimal confined space geometries for DMP adsorption in NMP, porous carbons with systematically varied microporous architectures were evaluated. DFT-optimized geometries reveal molecular dimensions of 3.4 × 5.0 × 6.2 $Å^3$ for NMP and 3.9 × 5.9 × 6.5 $Å^3$ for DMP. Consequently, pores must exceed 5.9 Å to ensure both size compatibility and confinement-enhanced effects, thereby enabling molecular recognition and selective capture of DMP.[30] Conceptually, the pore confinement effect represents a "selective spatial constraint", where pore size dictates molecular accessibility and pore volume governs adsorption capacity; thus, pore size serves as the principal determinant of selectivity. To delineate the optimal micropore range, a series of carbon materials with distinct micropore structures were synthesized, and their impact on DMP adsorption was systematically evaluated. Dominant micropore sizes in these materials included 6.8 Å, 7.3 Å, 8.0 Å, 10.0 Å, and 10.3 Å. Subsequent analysis of adsorption performance differences was conducted to assess DMP selectivity and identify the most favorable pore size for NMP systems.

For the β-CD-600, β-CD-700, and β-CD-800 series, primary micropore sizes were 6.8 Å and 7.3 Å. Comparative analysis of DMP adsorption behavior elucidated the effect of pore size on selective adsorption. Adsorption isotherms measured at 25 °C (Fig. 2c and S10) were fitted using Langmuir and Freundlich models (Tables S5–S11). All three carbons exhibited superior fitting to the Langmuir model ($R^2 > 0.99$), indicating monolayer adsorption with homogeneous sites. Notably, β-CD-700 and β-CD-800, dominated by 7.3 Å pores, achieved DMP capacities of 160.3 mg g^{-1} and 142.7 mg g^{-1}, respectively, whereas β-CD-600 (6.8 Å) yielded only 61.7 mg g^{-1}. Enlarging the pore size from 6.8 Å to 7.3 Å more than doubled the adsorption capacity, demonstrating that 7.3 Å pores provide optimal confinement for high-selectivity DMP adsorption in NMP. Following comparative analysis of 6.8 Å and 7.3 Å micropores, the findings confirm that 7.3 Å is the optimal pore size for the present system. To investigate whether larger micropores could further enhance DMP selectivity, the study expanded to porous carbons with larger pore sizes. The materials investigated included α-800 (predominantly 7.3 Å pores), α-700 (mainly 8.0 Å and 10.9 Å pores), and γ-600 (exclusively 10.9 Å pores). The DMP adsorption performance of these materials was evaluated to elucidate the impact of 7.3 Å, 8.0 Å, and 10.9 Å micropores on adsorption selectivity. Corresponding DMP adsorption isotherms for γ-600, α-700, and α-800 are presented in Fig. 2d and S11. Adsorption data fitted to both Langmuir and Freundlich models indicated that the Langmuir model provided a superior fit (Table S13), confirming its suitability for describing DMP adsorption behavior in these materials. Maximum DMP adsorption capacities were 45.3 mg g^{-1}, 73.9 mg g^{-1}, and 168.1 mg g^{-1} for γ-600, α-700, and α-800, respectively. Notably, as micropore size increased from 7.3 Å to 10.9 Å, adsorption capacity decreased markedly from 168.1 mg g^{-1} to 45.3 mg g^{-1}, indicating that 7.3 Å is the most favorable pore size for selective DMP adsorption among the investigated micropores.

In the β-CD-derived series (β-CD-600, β-CD-700, and β-CD-800), predominant micropores were centered at 6.8 Å and 7.3 Å. Adsorption measurements demonstrated that 7.3 Å pores create a more favorable confinement environment for selective DMP capture from NMP compared to 6.8 Å pores. A broader set of model materials, including α-800

(dominated by 7.3 Å pores with contributions from 8.0 Å and 10.9 Å), α-700 (mainly 8.0 Å and 10.9 Å pores), and γ-600 (exclusively 10.9 Å pores), further corroborated that 7.3 Å confinement is uniquely suited for selective DMP uptake (Fig. 2e). Interestingly, despite possessing a larger pore volume (0.29 $cm^3\ g^{-1}$) than α-800 (0.23 $cm^3\ g^{-1}$), β-CD-600 exhibited a significantly lower adsorption capacity (61.7 *vs.* 202.8 mg g^{-1}, Fig. 2f). This striking contrast demonstrates that geometric pore size alone does not fully capture the confinement effect. Unlike the conventional view emphasizing direct size matching between pores and adsorbates, our results reveal that confinement selectivity is governed by a more intricate structure–property relationship. Specifically, β-CD-600 contains interconnected 6.8 Å and 7.3 Å pores. The smaller 6.8 Å domains can simultaneously accommodate NMP and DMP, intensifying competitive adsorption and suppressing DMP preferential uptake. To rationalize this, we propose the concept of "end-capping" confinement, which posits that the smallest effective pore in a material should correspond to the optimal confinement size, ensuring that smaller pores do not compromise molecular selectivity. Beyond pore size distribution, pore volume plays a regulatory role in selective adsorption. Comparative studies of α-800 and β-800, which share similar pore size distributions, revealed a higher fraction of 7.3 Å pores in β-800 (0.201%) compared to α-800 (0.088%) (Fig. 2g). Adsorption isotherms of β-800 (Fig. 2d) fit well to the Langmuir model, yielding a maximum DMP uptake of 202.8 mg g^{-1}—20.6% higher than α-800 (168.1 mg g^{-1}). These findings highlight that, within the optimal 7.3 Å confinement, increasing the pore volume fraction significantly enhances selective adsorption capacity.

2.3.4 Kinetics and cyclic regeneration performance of β-800. To evaluate the adsorption efficiency of β-800, kinetic studies were conducted in NMP solutions containing DMP at concentrations of 296 and 450 mg kg^{-1} (Fig. 2h and S12). Initially, a rapid adsorption process was observed, followed by a gradual approach to saturation, with equilibrium achieved within approximately 180 minutes. This behavior reflects the high availability of accessible active sites during the initial stage, which gradually became saturated, thereby decelerating the adsorption rate. Increasing the initial concentration from 296 to 450 mg kg^{-1} resulted in a ~60% increase in adsorption capacity. Kinetic modeling revealed that the pseudo-second-order model provided a superior fit to the data (Table S13), with higher R^2 values and equilibrium capacities closely matching experimental results, indicating that the adsorption process was predominantly chemisorption-driven. Notably, the rate constant k_2 at 450 mg kg^{-1} (2.57×10^{-3} g $mg^{-1}\ min^{-1}$) was nearly an order of magnitude greater than that at 296 mg kg^{-1} (6.69×10^{-4} g $mg^{-1}\ min^{-1}$), attributed to reduced diffusion resistance and an enhanced concentration driving force at higher solute concentrations. Durability assessments of β-800 were conducted *via* cyclic regeneration tests at an initial DMP concentration of 400 mg kg^{-1}. After three consecutive adsorption–desorption cycles, the adsorption capacity declined only slightly, from 64.9 to 60.2 mg g^{-1} (Fig. 2i), demonstrating exceptional reusability and structural stability. To conduct a comprehensive evaluation of the competitive adsorption selectivity of β-800 for DMP and NMP, adsorption experiments were performed with an initial DMP concentration of 416 mg kg^{-1}, using internal standard gas chromatography for precise quantification. The peak area ratios of DMP and NMP in both the adsorbed and solution phases were monitored at equilibrium, yielding a separation factor (α) of 2.2. This result demonstrates that β-800 exhibits significantly higher selectivity for DMP compared to NMP within the studied concentration range, underscoring its potential for industrial applications in the separation of organic solvent mixtures. To systematically assess the DMP adsorption capacity of β-800 in NMP, comparative adsorption experiments were conducted under identical conditions (DMP concentration: 416 mg kg^{-1}) using metal–organic frameworks (MOFs) – HKUST-1 and UiO-66 – both exhibiting similar confinement effects. As depicted in Fig. S13, the adsorption capacity of HKUST-1 for DMP in NMP was negligible, yielding only 0.8 mg kg^{-1}, while UiO-66 displayed a higher capacity of 6.3 mg kg^{-1}. In contrast, β-800 exhibited a significant enhancement in adsorption capacity, reaching 22.5 mg kg^{-1}, thus outperforming both MOF-based materials. This marked performance disparity highlights the unique advantages of β-800 for the selective adsorption of DMP from NMP solutions, emphasizing its potential for efficient solvent purification applications.

2.4 Carbon materials for the mechanism of DMP adsorption in NMP

2.4.1 Interaction mechanism of surface functional groups with NMP/DMP. In evaluating the adsorption performance of carbon materials, it was observed that non-porous carbons, including α-CD-230, β-CD-230, and γ-CD-230, exhibited negligible DMP adsorption in NMP. These experimental results preliminarily indicate that the pore structure of the carbon materials is the key factor governing the selective adsorption of DMP from NMP. Although the surface functional group content is extremely low after high-temperature activation (Table S4), we conducted DFT calculations to evaluate the interactions between potential surface functional groups and NMP/DMP. This was done to definitively rule out any potential influence of surface chemistry on the adsorption performance and to clarify the role of these functional groups in the adsorption process. Carbon structures functionalized with hydroxyl (–OH) and carboxyl (–COOH) groups were modeled as C–OH and C–COOH, respectively. The interaction models C–OH-DMP and C–OH–NMP were employed to analyze DMP and NMP adsorption on C–OH, while C–COOH–DMP and C–COOH–NMP represented adsorption on C–COOH. The calculated adsorption energies are summarized in Fig. 3. For C–OH, the adsorption

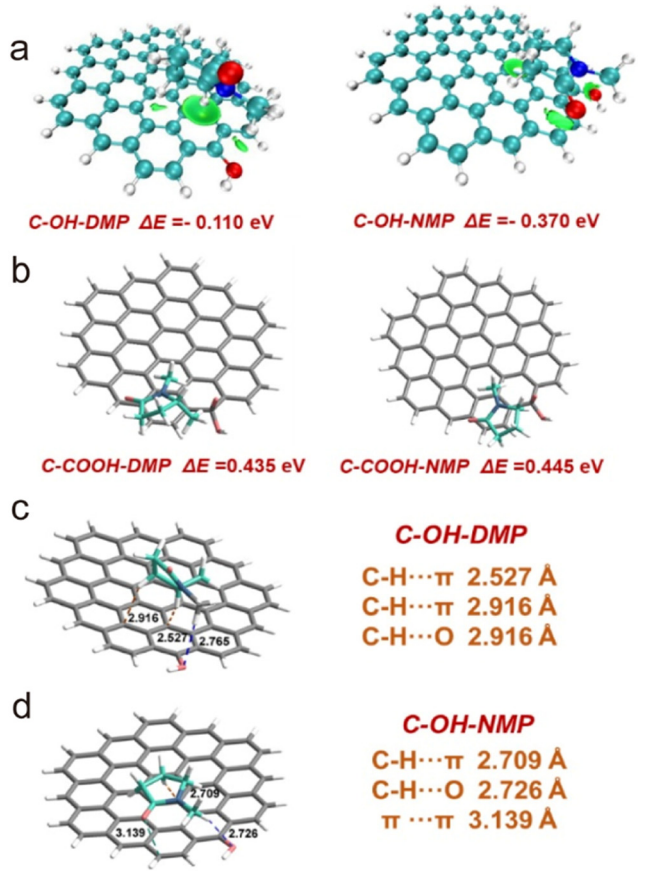

Fig. 3 DFT-calculated adsorption strength of (a) hydroxyl groups on porous carbon for NMP and DMP; (b) carboxyl groups on porous carbon for NMP and DMP; interaction analysis of hydroxyl groups with (c) NMP and (d) DMP on porous carbon.

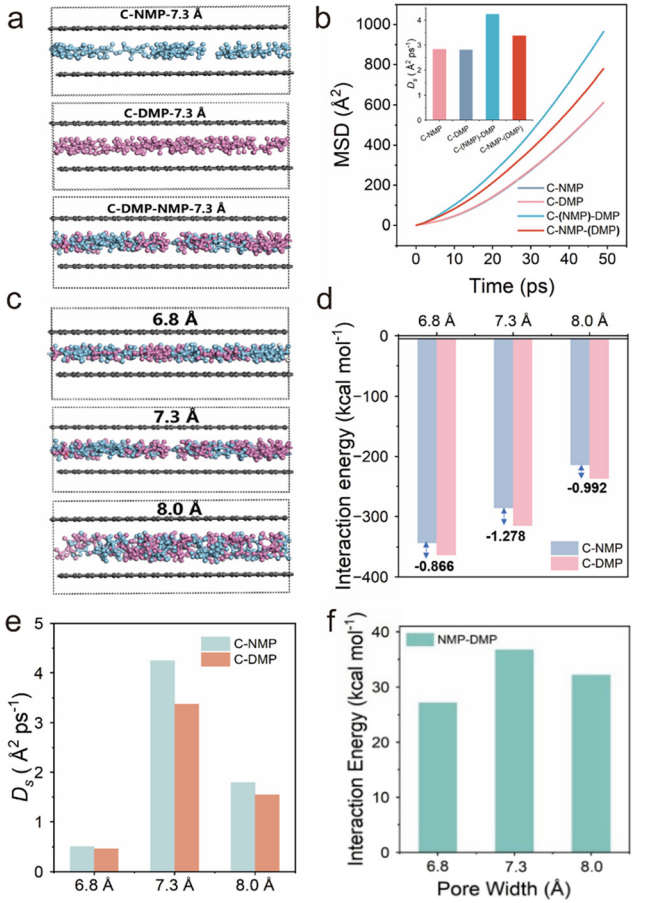

Fig. 4 (a) Molecular dynamics simulations of diffusion behavior in carbon materials with a pore size of 7.3 Å (0.73 nm) for NMP and DMP as individual components and as a binary mixture; (b) comparison of diffusion coefficients of NMP and DMP in carbon materials with a pore size of 7.3 Å, derived from molecular dynamics simulations; (c) molecular dynamics simulations of diffusion behavior in carbon materials with varying pore sizes (6.8 Å, 7.3 Å, and 8.0 Å) for the binary mixture of NMP and DMP; (d) interaction energies between carbon materials and NMP or DMP at varying pore sizes (6.8 Å, 7.3 Å, and 8.0 Å), calculated *via* molecular dynamics simulations; (e) comparison of diffusion coefficients of NMP and DMP in carbon materials with pore sizes of 6.8 Å, 7.3 Å, and 8.0 Å, derived from molecular dynamics simulations; (f) intermolecular interaction strengths of NMP and DMP in carbon materials with pore sizes of 6.8 Å, 7.3 Å, and 8.0 Å, calculated *via* molecular dynamics simulations.

energies for DMP and NMP were −0.110 eV and −0.370 eV, respectively. In contrast, C–COOH exhibited positive adsorption energies of 0.435 eV (DMP) and 0.445 eV (NMP), indicating negligible adsorption affinity. These results suggest that hydroxyl groups in C–OH demonstrate stronger interactions with NMP than with DMP, as evidenced by the lower adsorption energy of NMP. Conversely, the positive adsorption energies of C–COOH confirm its inability to effectively adsorb either DMP or NMP. Thus, the lack of selective DMP adsorption by α-CD-230, β-CD-230, and γ-CD-230 in NMP is rationalized. To further characterize the interaction mechanisms, the Hirshfeld partition-based independent gradient model was applied to visualize C–OH–NMP/DMP interactions. As illustrated in Fig. 3a and b, the interactions between C-OH and both NMP and DMP were dominated by weak van der Waals forces (visualized in green). Fig. 3c and d reveal that C-OH-NMP interactions involve C–H···O, C–H···π, and π···π stacking with bond lengths of 2.726 Å, 2.709 Å, and 3.139 Å, respectively. For C–OH–DMP interactions, C–H···O and C–H···π interactions were observed with bond lengths of 2.765 Å, 2.916 Å, and 2.527 Å, respectively. These results demonstrate that the trace functional groups present in the carbon material neither enhance the adsorption strength of the adsorbent toward DMP in NMP nor promote its selectivity, further confirming that the predominant factor governing the selective adsorption in porous carbon materials is their unique and abundant pore structure.

2.4.2 Diffusion behavior of NMP and DMP in single- and mixed-component systems within nanoporous carbon. The adsorption of DMP from NMP by carbon materials exhibits strong pore-size dependence, yet the underlying mechanism —specifically whether this dependence arises from competitive adsorption between NMP and DMP—remains unresolved. To address this, MD simulations were performed to investigate the diffusion behavior of NMP and DMP in 7.3 Å-wide nanopores under both single-component and mixed-

component conditions. By comparing diffusion coefficients under these scenarios, the potential for competitive adsorption effects could be directly evaluated. A bilayer graphene interlayer spacing was employed as the structural model to simulate microporous environments with well-defined pore sizes. NMP and DMP molecules, either individually or as a mixture, were confined within the interlayer region and equilibrated for 50 ps. The resulting adsorption configurations were denoted as C–NMP, C–DMP, and C–NMP–DMP (Fig. 4a). In this notation, C–(NMP)–DMP represents the diffusion of NMP in the mixed-component system, while C–NMP–(DMP) denotes the diffusion of DMP under identical conditions. As illustrated in Fig. 4b, diffusion coefficients were calculated from the mean square displacement (MSD) profiles post-equilibration. For single-component systems, the diffusion coefficients of NMP and DMP were 2.83 $Å^2$ ps^{-1} and 2.81 $Å^2$ ps^{-1}, respectively. Notably, in the mixed-component system, these values increased to 4.25 $Å^2$ ps^{-1} for NMP and 3.38 $Å^2$ ps^{-1} for DMP. This enhancement is attributed to competitive adsorption at identical sites, which induces mutual steric exclusion and thereby enhances diffusivity. These findings provide unequivocal evidence of competitive adsorption between NMP and DMP in confined carbon nanopores.

2.4.3 Interaction energy between NMP/DMP and adsorbents with different pore sizes. To elucidate the influence of pore size on the selective adsorption of DMP from NMP and provide molecular-level insights into experimental observations, molecular dynamics simulations were conducted to evaluate the diffusion behaviors of NMP and DMP in carbon adsorbents with pore sizes of 6.8, 7.3, and 8.0 Å. Previous adsorption experiments have established 7.3 Å as the optimal pore size for confinement. This study focuses on the interaction energies of NMP and DMP with the adsorbents and further explores the molecular mechanism underlying the "end-capped" confinement effect. The adsorption equilibria of NMP/DMP mixtures at different pore sizes are presented in Fig. 4c, with corresponding interaction energies summarized in Fig. 4d. At 6.8 Å, the interaction energies with NMP and DMP are −373.73 and −363.72 kcal mol^{-1}, respectively. For 7.3 Å pores, the values are −286.11 kcal mol^{-1} (NMP) and −315.0 kcal mol^{-1} (DMP), while at 8.0 Å, they decrease to −214.22 kcal mol^{-1} (NMP) and −234.09 kcal mol^{-1} (DMP). These results demonstrate that the adsorbent interacts favorably with both components across all pore sizes, indicating competitive adsorption between NMP and DMP. Importantly, the interaction energy with DMP consistently exceeds that with NMP at all pore sizes. This trend can be rationalized by the higher mobility of NMP molecules, which diffuse more rapidly and thus exhibit weaker confinement-induced interactions. In contrast, the slower diffusion of DMP leads to stronger binding within confined environments, particularly in smaller pores. Consequently, the adsorbent exhibits selective affinity for DMP, with the strongest preference observed at 7.3 Å, corroborating experimental findings. Collectively, these results confirm that pore size critically governs the thermodynamic mechanism of selective DMP adsorption from NMP. The enhanced interaction at 7.3 Å underscores the role of appropriately sized micropores in maximizing confinement effects and enabling efficient molecular discrimination.

The interaction energy data were systematically analyzed to assess the adsorbent's performance for DMP adsorption in NMP across different pore sizes. The interaction energy differences between DMP and NMP at 6.8, 7.3, and 8.0 Å pores were calculated as −0.866, −1.278, and −0.992 kcal mol^{-1}, respectively (Fig. 4d). Notably, the largest energy difference (−1.278 kcal mol^{-1}) at 7.3 Å corresponds to the highest DMP selectivity, attributed to the adsorbent's stronger differentiation between DMP and NMP. This preferential interaction enables DMP molecules to occupy adsorption sites more efficiently, thereby enhancing selectivity. The confinement effect was most pronounced at 7.3 Å, followed by 8.0 Å, and was weakest at 6.8 Å. These computational results align with experimental adsorption data, emphasizing the critical role of pore size in modulating adsorption selectivity.

To validate the "end-capped" confinement space concept, interaction energies of NMP and DMP were analyzed at 6.8 and 7.3 Å pores during mixed-component diffusion. A clear trend emerged as pore size decreased from 7.3 to 6.8 Å: interaction energies with both NMP and DMP systematically increased, indicating stronger adsorbent–molecule interactions in smaller pores. Nitrogen adsorption–desorption experiments revealed interconnected pore channels, supporting the hypothesis that optimal confinement spaces enhance molecular uptake efficiency. At 6.8 Å, the system reached its most stable equilibrium with interaction energies of −373.73 kcal mol^{-1} (NMP) and −363.72 kcal mol^{-1} (DMP). While NMP interactions were weakest at this pore size, the stronger DMP binding led to increased adsorption competition. This competition caused NMP molecules to preferentially occupy adsorption sites, reducing DMP selectivity. Together, computational and experimental data robustly confirm the pivotal role of "end-capped" confinement spaces in achieving highly selective DMP adsorption from NMP.

2.4.4 Diffusion dynamics of NMP and DMP in adsorbents with different pore sizes. Thermodynamic interaction energy variations primarily determine the selective affinity of adsorption sites. However, within the complex pore networks of porous adsorbents, the diffusion of NMP and DMP across pores of different sizes is jointly governed by thermodynamic interactions and competing mass transfer pathways. To investigate this interplay, we systematically evaluated the diffusion dynamics of NMP and DMP in pores of 6.8, 7.3, and 8.0 Å (Fig. 4e). In 6.8 Å pores, NMP and DMP exhibit diffusion coefficients of 0.50 $Å^2$ ps^{-1} and 0.46 $Å^2$ ps^{-1}, respectively. At 7.3 Å, these values increase significantly to 4.25 $Å^2$ ps^{-1} (NMP) and 3.38 $Å^2$ ps^{-1} (DMP), while in 8.0 Å pores, the coefficients decrease to 1.79 $Å^2$ ps^{-1} (NMP) and

1.54 Å^2 ps^{-1} (DMP). These results demonstrate that both molecules diffuse most efficiently in 7.3 Å pores, a phenomenon that accelerates adsorption equilibrium establishment, mitigates internal concentration gradients, and reduces mass transfer resistance, thereby enhancing overall adsorption efficiency. Across all examined pore sizes, NMP consistently shows higher diffusion coefficients than DMP. This disparity stems from NMP's smaller molecular size, which encounters reduced steric hindrance during transport, enabling faster pore traversal. In contrast, larger DMP molecules diffuse more slowly and are more prone to selective adsorption within pores.

An anomalous diffusion behavior was observed. Contrary to the expectation that larger pores facilitate faster transport, our calculations revealed that the diffusion rate in 7.3 Å pores exceeds that in 8.0 Å pores, highlighting that at the angstrom scale, increased pore size does not necessarily correlate with enhanced diffusivity. While the previous discussion focused on pore–adsorbate structural relationships, we further investigated intermolecular interactions between the solvent (NMP) and adsorbate (DMP) to rationalize this deviation. As shown in Fig. 4f, the calculated interaction energies are 27.22 kcal mol^{-1} (6.8 Å), 36.75 kcal mol^{-1} (7.3 Å), and 32.16 kcal mol^{-1} (8.0 Å). The positive values indicate repulsive forces between molecules. Notably, the maximum repulsion occurs at 7.3 Å pores, which enhances the mean square displacement (MSD) of unstably adsorbed molecules. This increased molecular mobility accounts for the unexpectedly high diffusion rates of both NMP and DMP in 7.3 Å pores.

3 Conclusion

This study demonstrates that cyclodextrin-derived carbons can achieve sub-angstrom-level molecular discrimination between NMP and DMP through precise pore-size engineering. By employing hydrothermal carbonization followed by pyrolysis, carbons with tunable pore architectures were synthesized, where distinct decomposition and graphitization pathways govern the final pore structural characteristics. Comprehensive analysis reveals that selective adsorption is predominantly driven by pore confinement effects rather than surface functional group interactions. A pore size of 7.3 Å was identified as the optimal confinement space for achieving maximum DMP selectivity. Complementary DFT and MD simulations further demonstrate that surface –OH and –COOH groups contribute minimally to the separation process, while the 7.3 Å pore exhibits synergistic thermodynamic and kinetic advantages that synergistically enhance DMP adsorption selectivity. These findings establish a well-defined structure–property relationship for cyclodextrin-derived carbons, positioning precise pore-size engineering as a fundamental design principle for sub-angstrom molecular separations. This work provides critical insights for the development of advanced adsorbent materials in selective adsorption, precision purification, and molecular sieving technologies.

4 Experimental section

4.1 Chemicals

The α-CD, β-CD, and γ-CD used in this study were of analytical reagent (AR) grade (≥99.0%) and were acquired from Shanghai Aladdin Biochemical Technology Co., Ltd. Starting materials and reagents, such as NMP (99%) and DMP (99%), were purchased from Sigma-Aldrich and were used as received, without further purification, unless otherwise specified. Concentrated hydrochloric acid was procured from Xilong Scientific Co., Ltd.

4.2 Synthetic procedures

4.2.1 Hydrothermal synthesis of carbon materials. A 6 g quantity of α-cyclodextrin (α-CD), β-cyclodextrin (β-CD), or γ-cyclodextrin (γ-CD) was dissolved in 60 mL of deionized water. Following dissolution, 160 μL of concentrated hydrochloric acid was introduced to the solution. To ensure homogeneity, the mixture was sonicated for 15 minutes and subsequently transferred into a PTFE-lined stainless-steel autoclave. Hydrothermal carbonization was carried out at 230 °C for 20 hours, after which the reactor was cooled to ambient temperature under natural cooling conditions. The resulting suspension was centrifuged to separate the solid carbon precursors from the liquid phase. The solid products were repeatedly washed with deionized water at 80 °C until the filtrate reached clarity and neutrality. Finally, the washed solids were dried under vacuum at 100 °C for 12 hours. The synthesized carbon materials were systematically designated based on the precursor type and synthesis temperature. For instance, the carbon material derived from α-CD at 230 °C was labeled as α-CD-230.

4.2.2 High-temperature activation of hydrothermal carbon materials. To introduce microporosity in the carbon matrix, 1 g of α-CD-230, β-CD-230, or γ-CD-230 was loaded into a ceramic crucible and calcined in a tubular furnace under a nitrogen atmosphere. The temperature was linearly increased at a rate of 5 °C min^{-1} to a final temperature of 800 °C, held constant for 2 hours to complete the carbonization process, and then allowed to cool to ambient temperature under natural cooling conditions. The resulting activated carbon materials were systematically labeled as α-CD-800, β-CD-800, and γ-CD-800, respectively, according to their precursor type and calcination temperature.

4.2.3 High-temperature pyrolysis for carbon material preparation. To prepare porous carbon materials *via* direct pyrolysis, approximately 1 g of α-cyclodextrin (α-CD), β-cyclodextrin (β-CD), or γ-cyclodextrin (γ-CD) was loaded into a ceramic crucible and pyrolyzed in a tubular furnace under a nitrogen atmosphere. The temperature was linearly increased at a rate of 5 °C min^{-1} to a target temperature

range of 500–800 °C, held constant for 2 hours to complete the pyrolysis process, and then cooled to ambient temperature under natural cooling conditions. The resulting porous carbon materials were systematically labeled as α-800, β-800, and γ-800, respectively, according to the precursor type and final pyrolysis temperature.

4.3 Characterization of materials

We studied the surface area and porosity of the prepared carbon materials through a nitrogen sorption test at 77 K on a Micromeritics ASAP 2020 HD88, and all samples were pretreated under a high vacuum at 120 °C for 2 h before analysis; the surface areas were obtained by the Brunauer–Emmett–Teller (BET) method based on the adsorption data, and the porosities were acquired by the Non-Local Density Functional Theory (NLDFT) method. Fourier transform infrared (FT-IR) spectroscopy was performed using a Nicolet iS50 spectrometer with a scanning range of 400–4000 cm^{-1}. Raman spectroscopy was measured using an Invia Reflex Raman spectrometer with a light source of 532 nm, a testing wavelength range of 100–2000 cm^{-1}, a laser intensity of 1%, and 4 scans. The PXRD data was measured on an X'Pert-3 X-ray diffractometer using Cu K α line (λ = 1.5418 Å) at 45 kV 40 mA^{-1} under 45 kV 40 mA^{-1} conditions, with a step size of 5° min^{-1} and steps of 5–50° within 9 minutes. The oxygen-containing functional groups within the porous carbon materials were determined by the elemental analysis (EA) using a Vario EL cube element analyzer (Elementar).

4.4 Evaluation of adsorption performance

The adsorption performance was assessed through static adsorption experiments. In the experiment, 10 mg of the adsorbent material was placed in a 50 mL centrifuge tube, to which 10 g of an NMP solution containing a specific concentration of GBL was added. After sealing the centrifuge tube, the mixture was subjected to isothermal shaking adsorption for 24 hours under constant temperature (25 °C) and shaking speed (200 rpm). The concentrations of GBL and DMP in NMP were quantified using gas chromatography with a DB-5 column and a hydrogen flame ionization detector. Toluene was employed as the internal standard, and calibration curves for GBL and DMP were constructed (Fig. S1). The adsorption capacity (Q_e, mg g^{-1}) was calculated from the experimental data using formula (1).

$$Q_e = (C_0 - C_e) \times M_{NMP}/m_a \quad (1)$$

Q_e (mg g^{-1}) denotes the equilibrium adsorption capacity; C_0 (mg kg^{-1}) and C_e (mg kg^{-1}) represent the initial and equilibrium concentrations of DMP, respectively; M (g) refers to the mass of the NMP solution containing DMP; and m (mg) corresponds to the mass of the adsorbent.

The separation factor (α) was calculated using eqn (2).

$$\alpha = \frac{S_{DMP}/S_{NMP}}{S'_{DMP}/S'_{NMP}} \quad (2)$$

α indicates the selectivity of the adsorbent for DMP and NMP. Adsorption performance was assessed using gas chromatography with an internal standard method. In this method, S_{DMP} and S_{NMP} represent the peak areas of DMP and NMP in the adsorbent, respectively, while S'_{DMP} and S'_{NMP} correspond to the peak areas of DMP and NMP in the adsorbent after adsorption.

To evaluate adsorption isotherms and kinetics, 10 mg of the adsorbent was dispersed in a 50 mL centrifuge tube containing 10 g of NMP solution with varying DMP concentrations. The tubes were sealed and agitated on an orbital shaker at 200 rpm and 25 °C for 24 h. The equilibrium data were fitted to the Langmuir and Freundlich isotherm models, while the kinetic data were analyzed using pseudo-first-order and pseudo-second-order models.

4.5 Gas chromatographic analysis

GC analysis was performed using an Agilent 8890 GC system. The analysis involved headspace injection, which was preceded by incubating the samples at 110 °C for 10 min. Following incubation, headspace injection was carried out for 5 min at a pressure of 10 kPa. The mass of the substance within the container is around 0.02 g, and the container has a total capacity of 20 mL. The GC method that was used was as follows: The oven was set to operate for 22 min, with a ramping period of 10 °C min^{-1} increments from 50 °C to 250 °C and a 2 min hold; the injection temperature was 250 °C; the detector temperature was 250 °C with flow rates of 30 mL min^{-1} for nitrogen, 400 mL min^{-1} for air, and 40 mL min^{-1} for make-up; the flow rate of the carrier gas, helium, was 3.0 mL min^{-1}. The GC exhibited a detection limit of 1.2 pg C s^{-1}. Quantification was based on an internal standard method using toluene. The calibration curves for toluene and DMP were established over the concentration ranges of 0–2500 mg kg^{-1} and 0–3600 mg kg^{-1}, respectively, and exhibited excellent linearity with correlation coefficients (R^2) exceeding 0.999.

4.6 DFT simulation

The effect of surface functional groups on the adsorption behavior of carbon-based materials was systematically investigated through DFT simulations. Structural optimizations were carried out using the B3LYP functional in combination with the def2-SVP basis set for C, H, O and N atoms, with dispersion corrections included. Single-point energy calculations were performed using the PBE1PBE functional together with the def2-TZVP basis set to evaluate the interaction energies among these atoms.[32–34] All computational outcomes were subjected to further analysis *via* the Multiwfn program, and the adsorption energies of the adsorbents were evaluated according to the equations provided below:[35]

$$E = E_{(\text{adsorbents–adsorbates})} - E_{(\text{adsorbents})} - E_{(\text{adsorbates})} \quad (3)$$

4.7 Molecular dynamics simulation

To elucidate the molecular-level mechanisms underlying the selective adsorption of DMP in NMP, molecular dynamics (MD) simulations were conducted, employing the interlayer spacing of bilayer graphene as a representative model for the micropores in porous carbon. A series of confined adsorption systems were established on the basis of experimental data concerning adsorption selectivity. The adsorption capacity of DMP was quantified, while excess NMP was introduced to simulate realistic solvent conditions. A comprehensive MD model was constructed to simulate the dynamic competitive adsorption between DMP and NMP within confined environments.[36] In this study, the geometries of NMP and DMP molecules were first optimized using the DMol^3 module with the GGA–PBE functional. The convergence criteria for energy, force, and displacement were set to 1.0×10^{-5} Ha, 0.002 Ha Å^{-1}, and 0.005 Å, respectively, with a maximum of 500 iterations, yielding the most stable molecular conformations. A graphene slab was then constructed by expanding the unit cell to include 576 carbon atoms (lattice parameters: a = 44.28 Å, b = 39.36 Å). The interlayer spacing along the Z-axis was tuned to 6.8, 7.3, and 8.0 Å to obtain activated carbon models with different pore sizes, which were designated as C6.8, C7.3, and C8.0, respectively. Based on the experimentally measured saturated adsorption capacity of DMP (Q = 168 mg g^{-1}), the corresponding saturation loading was calculated to be approximately 20.52 molecules. To ensure the number of adsorbates remained below the maximum capacity while enabling competitive adsorption in mixed systems, 15 NMP and 15 DMP molecules were introduced into the C6.8, C7.3 and C8.0 carbon models, with single-component NMP and DMP adsorption on C7.3 used as controls. All five systems were then optimized using the Forcite module, with convergence thresholds of 2.0×10^{-5} kcal mol^{-1} for energy, 0.001 kcal mol^{-1} Å^{-1} for force, and 1.0×10^{-5} Å for displacement, and a maximum of 1000 iterations to achieve minimum-energy configurations. Subsequently, molecular dynamics simulations were performed under the NVT ensemble using the COMPASSIII force field. The carbon layers were fixed, while the system was maintained at 298.15 K with the Nose thermostat and Andersen barostat. A timestep of 1 fs and a total of 200 000 steps (200 ps) were applied, and trajectory snapshots were saved every 1000 steps after equilibration. Once the system energy had stabilized, interaction energies were calculated using ($E_{\text{int}} = E_{\text{total}} - E_{\text{NMP/DMP}} - E_{\text{C}}$). Finally, the mean square displacement (MSD) of NMP and DMP molecules was analyzed over the 175–200 ps time window, and the corresponding diffusion coefficients were obtained to elucidate the influence of pore size on molecular diffusion and adsorption behavior.

Author contributions

Rongkai Cui: conceptualization, data curation, investigation and writing – original draft; Minlei Yin: formal analysis, investigation, software, data curation and methodology; Xiaoyan Chen: investigation and validation; Xiaoyu Lou: software and validation; Chen Yang: formal analysis and validation; Ting Qiu: project administration, resources, supervision and funding acquisition; Jie Chen: supervision, resources and writing – review & editing.

Conflicts of interest

The authors declare no conflict of interest.

Data availability

The data supporting this article are available within the article and its supplementary information (SI). Supplementary information: the SI contains [additional experimental data, methodological details, and supporting figures referenced in the main text.]. See DOI: https://doi.org/10.1039/d5im00266d.

Acknowledgements

This work was supported by the National Natural Science Foundation of China (Grant No. 22478077, 22578065, 22278077 and 22508223), Natural Science Foundation of Fujian Province for Excellent Young Scholars Fund (Grant No. 2025J09025) and Natural Science Foundation of Fujian Province (Grant No. 2025J08356). We also greatly acknowledge support from State Key Laboratory of Green and Efficient Development of Phosphorus Resources.

References

1 M. Liu, G. Wang, F. Zhao, W. Li, G. Zhu, G. Liang, W. Jian, L. Liao and G. Lv, Advances in purification technologies and applications of high-purity quartz resources, *Prog. Nat. Sci.*, 2025, **35**, 51–64.
2 G. Isella, M. Virgilio, R. Loo, O. Nakatsuka and G. Capellini, *Preface: Advances in semiconductor materials, technology, and applications*, Elsevier, 2024.
3 I. T. S. Heikkinen, C. Kauppinen, Z. Liu, S. M. Asikainen, S. Spoljaric, J. V. Seppälä, H. Savin and J. M. Pearce, Chemical compatibility of fused filament fabrication-based 3-D printed components with solutions commonly used in semiconductor wet processing, *Addit. Manuf.*, 2018, **23**, 99–107.
4 T. Nakano, T. Tanahashi, A. Imai, K. Yamana, T. Shimotsu, N. Takahashi, M. Shioguchi, Y. Matsuda and J. Kitano, Molecular contamination control technologies for high-volume production phase in high-NA 193 nm lithography, *Proc. SPIE*, 2007, **6519**, 65193I.
5 J. Ni, Q. Zhang, X. Zhang, Z. Sun and D. Bao, Detection method and common characteristics of waste solvent from semiconductor industry, *Molecules*, 2023, **28**, 5992.
6 B. M. Pastore, M. J. Savelski, C. S. Slater and F. A. Richetti, Life cycle assessment of N-methyl-2-pyrrolidone reduction strategies in the manufacture of resin precursors, *Clean Technol. Environ. Policy*, 2016, **18**, 2635–2647.

7 Y.-S. Yoon, H. Khil Shin and B.-S. Kwak, Ring conversion of γ-butyrolactone into N-methyl-2-pyrrolidone over modified zeolites, *Catal. Commun.*, 2002, **3**, 349–355.
8 S. Khlifi, J. Marrot, M. Haouas, W. E. Shepard, C. Falaise and E. Cadot, Chaotropic effect as an assembly motif to construct supramolecular cyclodextrin–polyoxometalate-based frameworks, *J. Am. Chem. Soc.*, 2022, **144**, 4469–4477.
9 Z. Qi, R. Cui, H. Lin, C. Ye, J. Chen and T. Qiu, Challenges and perspectives on using acidic ionic liquids for biodiesel production *via* reactive distillation, *Green Chem.*, 2024, **26**, 7718–7731.
10 B. Shan, S. Wang, Q. Xu, Y. Wang, P. Cui and F. Zhang, Design and multi-objective optimization of hybrid extractive distillation process for separating the toluene-methanol-water ternary azeotrope, *Sep. Purif. Technol.*, 2024, **336**, 126335.
11 J. Zhu, X. Lou, Y. Wang, Z. Xiong, J. Chen and W. Yan, Conjugated microporous poly(aniline)s for removal of low-concentration formaldehyde, *Chem. Eng. Sci.*, 2022, **248**, 117119.
12 S. A. Mohamed, R. Zheng, N. Zhu, D. Zhao and J. Jiang, A systematic approach for incorporating structural flexibility in high-throughput computational screening of metal–organic frameworks for xylene separation, *J. Am. Chem. Soc.*, 2025, **147**, 12251–12262.
13 Q. Wang, Y. Li, Z. Qiu, D. Zhou, L. Yang, X. Suo, X. Cui and H. Xing, Highly efficient separation of intermediate-size *m*-xylene from xylenes via a length-matched metal–organic framework with optimal oxygen sites distribution, *Angew. Chem.*, 2024, **136**, e202408817.
14 D. Tang, Z. Xiong, P. Lu, S. Wang, X. Chen, X. Lou, M. Zheng, S. Chen, C. Ye, J. Chen and T. Qiu, Lacunary polyoxometalate @ ZIF for ultradeep Pb(II) adsorption, *Chem. Eng. Sci.*, 2022, **262**, 118003.
15 L. Qiu, Z. Wang, Z. Liu, H. Li and Y. Feng, Nanopore confinement-driven synchronous enhancement of thermal and mechanical properties of phase change materials, *Angew. Chem.*, 2025, **137**, e202500957.
16 Z. Liu, C. Lou, J. Yuan, X. Tang, Y. Fan, J. Qi, R. Zhang, P. Peng, G. Liu, S. Xu and A. Zheng, Molecular self-gating inside a zeolite catalyst, *J. Am. Chem. Soc.*, 2025, **147**, 6126–6136.
17 X. Li, S. Yang, X. Yang, S. Zheng, Q. Xu, G. Zeng and Z. Jiang, Construction of a pore-confined catalyst in a vinylene-linked covalent organic framework for the oxygen reduction reaction, *ACS Catal.*, 2024, **14**, 17862–17870.
18 H. Huang, H. Wu, Y. Zhang and X. Feng, Polyhedral polymeric microparticles with interwoven 1 nm gyroid pores for precise adsorption and nanoconfined degradation, *ACS Nano*, 2025, **19**, 8926–8938.
19 X. Long, C. Feng, M. Liu, X. Li, Z. Huang, Y. Du, Y. Chen, S. Yang, G. Wang, D. Ding, W. Huang and R. Chen, PMS activation by hollow sulfur doped multilayer carbon shell wrapped CoFe alloy: Confined adsorption and surface activation, *J. Cleaner Prod.*, 2023, **425**, 138672.
20 G. Li, X. Guo, Y. Liu, J. Sun, H. Yang, Y. Zheng, X. Zhang, P. K. Chu, G. He and B. Gao, Revealing the "double-layer ionic monotonic adsorption" electrochemical ion storage mechanism of nano-confined porous carbon, *Chem. Eng. J.*, 2025, **520**, 165799.
21 J. Chen, W. Yan, E. J. Townsend, J. Feng, L. Pan, V. Del Angel Hernandez and C. F. J. Faul, Tunable surface area, porosity, and function in conjugated microporous polymers, *Angew. Chem., Int. Ed.*, 2019, **58**, 11715–11719.
22 Z. Zhou, F. Yu and J. Ma, Nanoconfinement engineering for enchanced adsorption of carbon materials, metal–organic frameworks, mesoporous silica, MXenes and porous organic polymers: A review, *Environ. Chem. Lett.*, 2022, **20**, 563–595.
23 S. Yu, J. He, Z. Zhang, Z. Sun, M. Xie, Y. Xu, X. Bie, Q. Li, Y. Zhang, M. Sevilla, M. M. Titirici and H. Zhou, Towards negative emissions: Hydrothermal carbonization of biomass for sustainable carbon materials, *Adv. Mater.*, 2024, **36**, 2307412.
24 K. Xiao, Z. Zhou, C. Ye, J. Chen and T. Qiu, Hydrogen bond induced acidic solids for effective esterification catalysis, *Chem. Eng. J.*, 2023, **478**, 147398.
25 Z. Zhou, X. Chen, J. Worth, C. Ye, J. Chen and T. Qiu, Hydrogen bond induced acidic liquids for efficient biodiesel production, *AIChE J.*, 2023, **69**, e18098.
26 B. Qin, T. Zhang, H. Chen and Y. Ma, The growth mechanism of few-layer graphene in the arc discharge process, *Carbon*, 2016, **102**, 494–498.
27 F. Su, H. Peng, H. Yin, C. Luo, L. Zhu, W. Zhong, L. Mao and D. Yin, Biowaste-derived hydrochar microspheres: Realizing metal-free visible-light photocatalytic oxidation of amines, *J. Catal.*, 2021, **404**, 149–162.
28 P. Zhang, Y. Chen, X. Song, H. Zhang, J. Cui and B. Wang, Preparation of hierarchical porous carbon from corncob hydrochar by KCl enhancing K_2CO_3 activation for electrode material of supercapacitor, *Chem. Eng. J.*, 2025, **503**, 157703.
29 Y. Gong, L. Xie, C. Chen, J. Liu, M. Antonietti and Y. Wang, Bottom-up hydrothermal carbonization for the precise engineering of carbon materials, *Prog. Mater. Sci.*, 2023, **132**, 101048.
30 K. Wang, F. Sun, H. Wang, D. Wu, G. Zhao and X. Su, Spatially confined carbonization-induced reorganization of microcrystals and nanopores in carbon framework for enhanced sodium plateau storage, *Adv. Energy Mater.*, 2025, **15**, 2405294.
31 M. Li, M. Sun, E. Mohammadian, Y. Ji, T. P. Blach, M. Ostadhassan, J. Wen, C. Wu and Z. Pan, Confinement effect in nanopores of shale and coal reservoirs: A review on experimental characterization methods, *Gas Sci. Eng.*, 2024, **123**, 205249.
32 X. Ji, Y. Liu, Z. Gao, H. Lin, X. Xu, Y. Zhang, K. Zhu, Y. Zhang, H. Sun and J. Duan, Efficiency and mechanism of adsorption for imidacloprid removal from water by Fe-Mg co-modified water hyacinth-based biochar: Batch adsorption, fixed-bed adsorption, and DFT calculation, *Sep. Purif. Technol.*, 2024, **330**, 125235.

33 M. Yin, C. Yang, D. Tang, S. Huang, X. Lou, R. Cui, C. Ye, J. Chen and T. Qiu, Revealing the mechanism behind the highly selective separation of 1,4-butyrolactone from n-methylpyrrolidone using nonporous adaptive crystals of perethylated pillar[5]arene, *Chem. Eng. J.*, 2024, **495**, 153508.
34 D. Tang, M. Yin, X. Du, Y. Duan, J. Chen and T. Qiu, Wettability tunable conjugated microporous poly(aniline)s for long-term, rapid and ppb level sequestration of Hg(II), *Chem. Eng. J.*, 2023, **474**, 145527.
35 R. Cui, F. Yin, W. Gong, N. Yan, S. Li, C. Ye, T. Qiu and J. Chen, A bioinspired heterogeneous catalyst for green and targeted transesterification of ethanol and dimethyl carbonate to ethyl methyl carbonate with high endurance, *Green Chem.*, 2025, **27**, 11167–11178.
36 W. Jian, W. Zhang, X. Wei, B. Wu, W. Liang, Y. Wu, J. Yin, K. Lu, Y. Chen, H. N. Alshareef and X. Qiu, Engineering pore nanostructure of carbon cathodes for zinc ion hybrid supercapacitors, *Adv. Funct. Mater.*, 2022, **32**, 2209914.